RSC Advances

PAPER

Check for updates

Cite this: *RSC Adv.*, 2024, **14**, 24226

Wide-direct-band-gap monolayer carbon nitride CN_2: a potential metal-free photocatalyst for overall water splitting

Qiang Lu,[a] Bofeng Zhang*[b] and Jiahe Lin *[a]

Two dimensional metal-free semiconductors with high work function have attracted extensive research interest in the field of photocatalytic water splitting. Herein, we have proposed a kind of highly stable monolayer carbon nitride CN_2 with an anisotropic structure based on first principles density functional theory. The calculations of electronic structure properties, performed using the HSE06 functional, indicate that monolayer CN_2 has a wide direct band gap of 2.836 eV and a high work function of 6.54 eV. And the suitable band edge alignment, high electron mobility ($\sim 10^3$ cm^2 V^{-1} s^{-1}) and visible-light optical absorption suggest that monolayer CN_2 has potential on visible-light photocatalytic water splitting at pH ranging from 0 to 14. Moreover, we have observed that uniaxial strain can effectively control the electronic structure properties and optical absorption of monolayer CN_2, which can further improve its solar to hydrogen efficiency from 9.6% to 16.02% under 5% uniaxial tension strain along the *Y* direction. Our calculations have not only proposed a new type of potential metal-free photocatalyst for water splitting but also provided a functional part with high work function for type-I and scheme-Z heterojunction applied in photocatalytic water splitting.

Received 30th June 2024
Accepted 29th July 2024

DOI: 10.1039/d4ra04756g

rsc.li/rsc-advances

1 Introduction

Two dimensional (2D) semiconductor photocatalysts applied in water splitting have received widespread research interest due to their high specific surface area and abundant reactive active sites caused by a unique atomic-scale thickness feature.[1–6] Motivated by it, much attention has been drawn to exploring new 2D semiconductors for photocatalytic water splitting. For completely photocatalytic water splitting, 2D semiconductors should have suitable band edge alignment to satisfy the band structure requirement of photocatalytic water splitting, including band gaps being larger than 1.23 eV and the valence band maximum (VBM) and conduction band minimum (CBM) relative to the vacuum level being higher than the reduction potential ($V_{H^+/H_2} = -4.44$ eV) and lower than the oxidation potential ($V_{OH^-/O_2} = -5.67$ eV), respectively.[7–10] In addition, to consider the pH ranging from 0 to 14, the band gaps of 2D semiconductor photocatalysts should be larger than 2.0 eV so as to guarantee the reduction reaction in photocatalytic water splitting.[11–14] Furthermore, large enough overpotential and strong visible light optical absorption are also essential for ensuring enough driven energy and relatively high solar conversion efficiency. Based on the above, a comprehensive 2D semiconductor photocatalyst for water splitting should have a wide band gap (>2.0 eV), high work function and favourable optical absorption.[15–19] Besides, a wide-band-gap 2D semiconductor with high work function can be adopted in type-II and Z-scheme van der Waals heterojunctions for photocatalytic water splitting.[20–28] Therefore, it is necessary for exploring more wide-band-gap 2D semiconductor photocatalysts with high work function and excellent optical absorption for photocatalytic water splitting.

A 2D material with high work function always means that it owns strong ability for binding electrons. To design the 2D material with high work function, one of elements that have high electronegativity should be contained, such as C, N, O and S elements. Typically, 2D carbon nitrides with economic and clean features are hot candidates for the application of photocatalytic water splitting.[29,30] 2D g-C_3N_4, one of most famous 2D carbon nitrides, has wide direct band gap, strong optical absorption in visible-light region and suitable band edge alignment for photocatalytic water splitting.[31–38] Besides, monolayer g-C_2N is also reported that have potential in the application of photocatalytic water splitting.[39] However, these two graphene-like 2D carbon nitrides do not own high enough work function, which is not beneficial for the oxidation reaction activity. Moreover, the graphene-like monolayer C_3N and some others graphene-like 2D carbon nitrides have small band gaps,[40,41] relative low work function and do not suitable for photocatalytic water splitting. The phenomenon is mainly cause by that the outmost electrons C atoms and even N atoms are not

[a]*School of Science, Jimei University, Xiamen, 361021, China. E-mail: linjiahe@jmu.edu.cn*

[b]*Department of Chemistry, College of Chemistry and Chemical Engineering, Xiamen University, Xiamen, 361005, China. E-mail: zhangbofeng@stu.xmu.edu.cn*

This article is licensed under a Creative Commons Attribution-NonCommercial 3.0 Unported Licence.

© 2024 The Author(s). Published by the Royal Society of Chemistry

fully saturated. On the contrary, the monolayer C_3N_2 owning four-bonded C atoms (sp^3 hybridization) and three-bonded N atoms (sp^3 hybridization) exhibits wide band gap, pretty high work function (~7.0 eV) and suitable band edges alignment for photocatalytic water splitting. Meanwhile, such the electronic structure properties of monolayer C_3N_2 reveals its great potential on being an important component in type-I and Z-scheme heterojunction for photocatalytic water splitting.[42] Therefore, to explore the new 2D carbon nitrides with high work function and wide band gap, the sp^3-C atoms and sp^3-N atoms should be fully contained.

In this paper, we have theoretically designed a new type of 2D carbon nitrides called monolayer CN_2 based on first-principles density functional theory (DFT). The stability of monolayer CN_2 was confirmed by the calculations of cohesive energy, phonon spectrum and *ab initio* molecular dynamics (AIMD) at 300 K and 400 K. The electronic structure properties of monolayer CN_2 were investigated through its band structure, density of state and work function, which indicated that monolayer CN_2 was a wide-direct-band-gap semiconductor with high work function. Moreover, its carrier mobility, optical absorption, band edge alignment relative to the vacuum level and solar to hydrogen (STH) efficiency were further studied to preliminarily evaluate the photocatalytic ability of monolayer CN_2 for water splitting. Finally, the uniaxial strain along *X* and *Y* direction were applied to monolayer CN_2 to study the strain effect on electronic structure properties, optical absorption and photocatalytic properties.

2 Computational details

All results in this paper were carried out by performing the calculations based on first-principles density functional theory (DFT). The Vienna *Ab Initio* Simulation Package (VASP) was used for the calculation of geometry optimization, band structures and optical absorption. The projector-augmented-wave (PAW) pseudopotentials were utilized with a 500 eV plane-wave cutoff energy.[43] The conventional cell of monolayer CN_2 were mainly used considering its anisotropic structure feature. The Brillouin zone sampling adopted $12 \times 8 \times 1$ gamma-centered *k*-point mesh.[44] A vacuum separation between neighbouring monolayers was over 20 Å. The Perdew–Burke–Emzerh of Generalized Gradient Approximation (GGA + PBE) was used for geometry optimization.[45] The monolayer CN_2 were relaxed until the internal stress was reduced to below 0.001 eV $Å^{-1}$, and the energy tolerance was set to be less than 1×10^{-8} eV per atom. The thermodynamic stability of monolayer CN_2 at 300 K and 400 K was simulated through *ab initio* molecular dynamics (AIMD) with using 96 atoms supercell and NVT canonical ensemble.[46] The total simulation time was set to 5 ps corresponding to 5000 simulation steps. The band structures and optical absorption spectra of monolayer CN_2 were calculated by using the Heyd–Scuseria–Ernzerh of hybrid functional (HSE06).[47] The VASPKIT code was used for post-processing data obtained from the VASP code.[48] The phonon dispersion spectrum of monolayer CN_2 was calculated using the linear response approach implemented in the Cambridge Series of Total Energy Package (CASTEP).[49] For phonon spectrum calculations, norm-conserving pseudopotentials and a plane-wave cutoff energy of 750 eV were employed, while other settings were consistent with those used in the VASP code.

3 Results and discussion

3.1 The structure and stability of monolayer CN_2

After sufficient structure optimization, the structure models of monolayer CN_2 are given in Fig. 1. In the monolayer CN_2, each C atom bond with two C atoms and two N atoms while each N atom bond with one C atom and two N atoms. It is clear that both the C and N atoms in the monolayer are sp^3 hybridization, which means the structure reasonability of monolayer CN_2. Learning from Fig. 1, we also can get that the structure of monolayer CN_2 is anisotropic reflecting atom alignment difference between *X* direction and *Y* direction shown in Fig. 1(a). And in order to study the anisotropic properties of monolayer CN_2 caused by its anisotropic structure, we carry out its conventional cell containing the lattice parameters, as shown in Fig. 1(d). Although the structure of monolayer CN_2 seems to be reasonable, the further studies about its energy, dynamic and thermodynamic stability are still sorely necessary. For the energy stability, we have calculated the cohesive energy (E_{coh}) of monolayer CN_2 as followed formula:

$$E_{coh} = \frac{E_{tot} - 4E_{atom}(C) - 8E_{atom}(N)}{12} \quad (1)$$

where E_{tot} is the total energy of monolayer CN_2, and the E_{atom}(C) and E_{atom}(N) are the energy of free C and N atoms, respectively. The calculation presents that the E_{coh} of monolayer CN_2 is −7.48 eV per atom, which is lower than that of monolayer C_2N and g-C_3N_4. So we consider such E_{coh} as an evidence for proving that monolayer CN_2 is energy stable. In addition, we have carried out the phonon spectrum of monolayer CN_2 that is shown in Fig. 2(a). It is noticed that there is not imaginary frequency in the phonon spectrum of monolayer CN_2, which indicates that monolayer CN_2 is dynamically stable. Moreover, the thermodynamic stability of monolayer CN_2 have been investigated by performing the AIMD simulation at 300 K and 400 K, which represent the room temperature and the temperature of boiling water, respectively. The Fig. 2(b) exhibits that, during AIMD simulation at 300 K and 400 K, the total energy of monolayer CN_2 do not have mutations and keep in a dynamic equilibrium process. Furthermore, the Fig. 2(c and d) present that, after 5 ps AIMD simulation at 300 K and 400 K, there are no dramatic changes in the structure of monolayer CN_2. Therefore, we confirm that monolayer CN_2 are thermodynamically stable at 300 K and 400 K.

3.2 The electronic structure, optical absorption and photocatalytic properties of monolayer CN_2

The projected band structure of optimized monolayer CN_2 were calculated by HSE06 hybrid function shown in Fig. 3(a and b). The Fig. 3(a and b) show that monolayer CN_2 is a wide-direct-band-gap semiconductor with a 2.836 eV band gap. And both the VBM and CBM are locating at *G* point. The such band gap is

© 2024 The Author(s). Published by the Royal Society of Chemistry

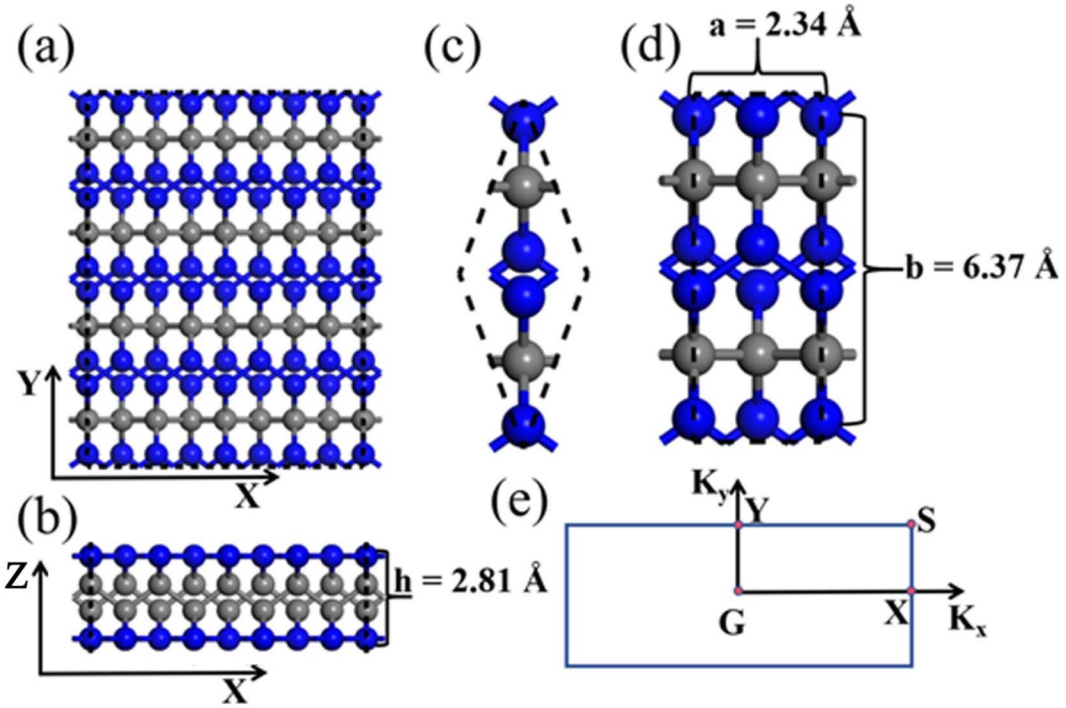

Fig. 1 (a) and (b) are the top and side view of monolayer CN_2 after full optimization, respectively. (c) and (d) are the primitive cell and conventional cell of monolayer CN_2, respectively. And the lattice parameters *a*, *b* and *h* of conventional cell are also exhibited (e) is the Brillouin zone containing main high symmetric points for the conventional cell of monolayer CN_2.

similar with the band gap of g-C_3N_4. Comparing Fig. 3(a) with Fig. 3(b), we find that the states near the VBM and CBM are mainly contributed by N atoms while there is minor contribution from C atoms. To further study the atomic orbital occupation of monolayer CN_2, we have calculated the projected density of states (PDOS), as shown in Fig. 4. The total density of states (TDOS) in the Fig. 4(a) indicates that the occupation peaks near the VBM and CBM are relatively low, which will be unfavorable for electron collective transition and lead to weak optical absorption in low energy region. The Fig. 4(a) also identify that the N atoms have major contribution on the states near the VBM and CBM and the situation of C atoms is opposite. Learning from Fig. 4(b and c), we find that the states near the VBM are mainly contributed by the p_z orbital for C atoms and the p_z orbital for N atoms. Additionally, the states near the CBM are mainly contributed by the p_z orbital for C atoms and the s orbital for N atoms. Based on the situation, we suppose that carrier would tend to transfer in the *Y* direction. And the further calculation about carrier mobility along *X* direction and *Y* direction have been performed in the next section to identify the conjecture.

The carrier mobility of monolayer CN_2 were estimated by the 2D deformation potential (DP) theory with considering its anisotropic properties. The carrier mobility was calculated by following equations:[50]

$$\mu = \frac{e\hbar^3 C_{2D}}{k_B T m^* m_d E_l^2} \quad (2)$$

$$m^* = \hbar^2 \left(\frac{d^2 E_k}{dk^2} \right)^{-1} \quad (3)$$

$$C_{2D} = 2[\partial^2 E/\partial(\Delta a/a_0)^2]/S_0 \quad (4)$$

$$m_d = \sqrt{m_X^* m_Y^*} \quad (5)$$

$$E_l = \partial E_{edge}/\partial(\Delta a/a_0) \quad (6)$$

where the μ is the carrier mobility, the C_{2D} is the effective elastic modulus, The *T* is 300 K, the *m** is effective mass along specific direction, the m_d is average effective mass, and the E_l is the deformation potential constants. For the C_{2D}, the a_0 is the lattice constant without strain, the Δa presents the deformation of a_0, the S_0 is the total area of structures without strain, and the *E* is the total energy with the strain along specific direction. For the E_l, the E_{edge} is the change of the CBM and VBM with the strain along specific direction. The results are shown in Table 1. We get that the electron mobility along *X* direction and *Y* direction are 88.4 and 754.1 $cm^2\ V^{-1}\ s^{-1}$, respectively. Additionally, the hole mobility along *X* direction and *Y* direction are 303.6 and 1009.2 $cm^2\ V^{-1}\ s^{-1}$. It can be observed that the carrier mobility along *Y* direction is higher than that along *X* direction, which confirms the above conjecture mentioned at the analysis of DOS. Moreover, there are relatively large differences between hole and electron mobility both along *X* direction and *Y* direction, which is conducive to the separation of photogenerated hole and electron in the photocatalytic process.

© 2024 The Author(s). Published by the Royal Society of Chemistry

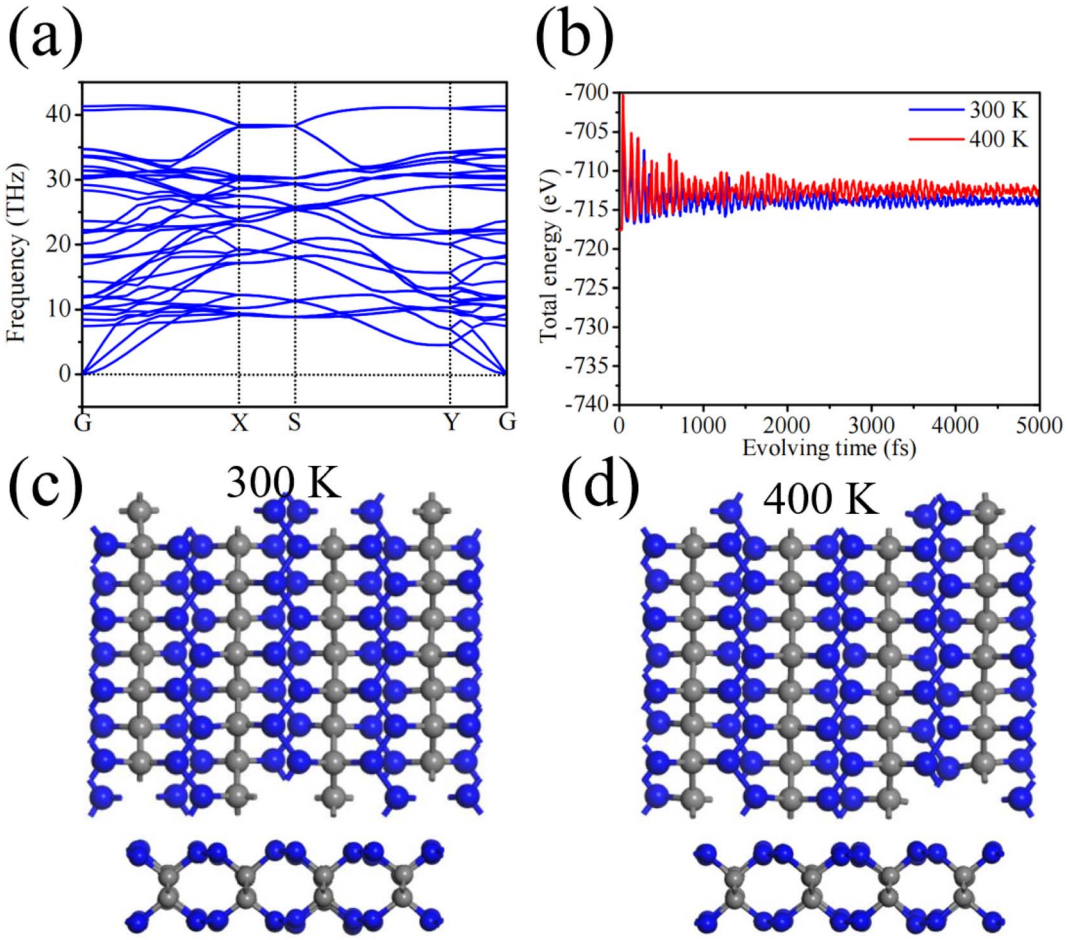

Fig. 2 (a) Is the phonon dispersion spectrum of monolayer CN_2. (b) Presents the total energy change of monolayer CN_2 in AIMD simulations at 300 K and 400 K. The (c) and (d) are the final structures of monolayer CN_2 after the AIMD simulations at 300 K and 400 K, respectively.

Due to the anisotropic electronic structure properties, the optical absorption properties of monolayer CN_2 will logically present anisotropic. The optical absorption spectra of monolayer CN_2 polarized in X direction and Y direction have been carried out by following formulas:

$$A(\omega) = 1 - e^{-\alpha(\omega)\cdot\Delta z} \tag{7}$$

$$\alpha(\omega) = \frac{\omega\varepsilon_2}{cn} \tag{8}$$

$$n = \sqrt{\frac{\sqrt{\varepsilon_1{}^2 + \varepsilon_2{}^2} + \varepsilon_1}{2}} \tag{9}$$

where $A(\omega)$ presents the optical absorbance, $\alpha(\omega)$ presents the absorption coefficient, ΔZ presents the primitive-cell size in the

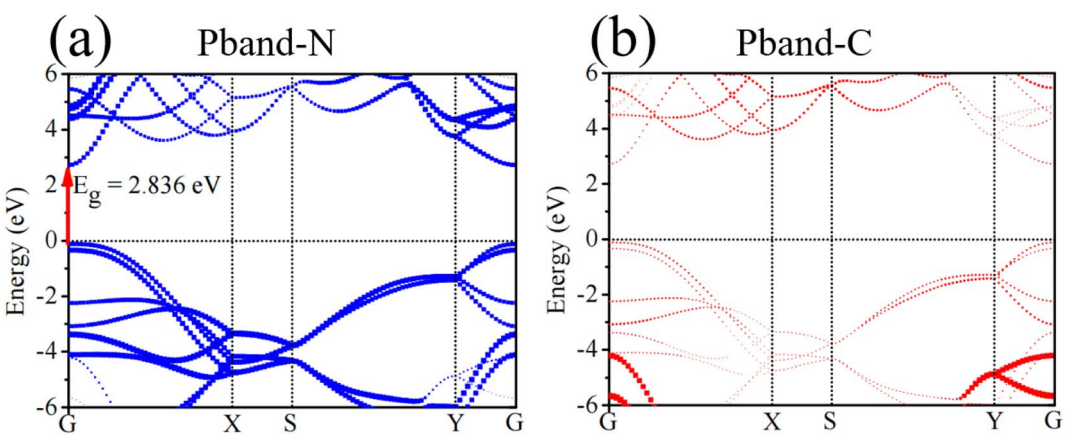

Fig. 3 (a) and (b) Are projected band structures contributed by N atoms and C atoms, respectively.

© 2024 The Author(s). Published by the Royal Society of Chemistry

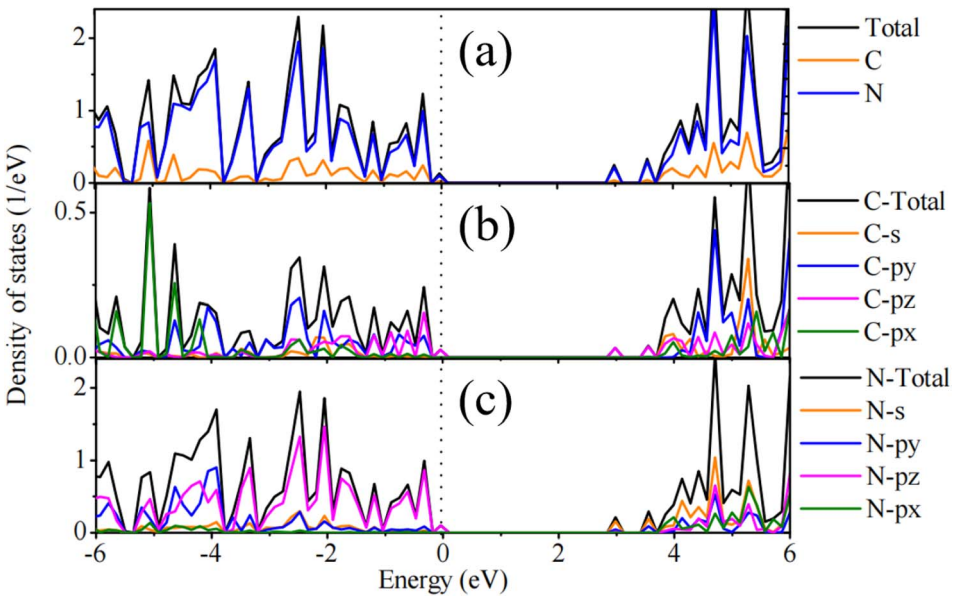

Fig. 4 (a) contain the TDOS of monolayer CN_2 and the PDOS contributed from C atoms and N atoms. (b) is the orbit-resolved PDOS of C atoms. (c) is the orbit-resolved PDOS of N atoms.

direction of vacuum layer, n presents the index of refraction, ε_1 and ε_2 respectively present the real and imaginary parts of their dielectric function, ω presents the incident light frequency, c presents the speed of light in vacuum. The result are shown in Fig. 5(a). It exhibits that monolayer CN_2 has optical absorption from violet region to ultraviolet region. In addition, we obtain that there exists anisotropic optical absorption reflecting on the optical absorption polarized in Y direction having much smaller optical gap and being much stronger in the region from ~3.0 eV to ~7.0 eV compared with that polarized in X direction. To explain the phenomenon, we then have calculated the transition dipole moment between highest VB and lowest CB presented in Fig. 5(b). It is well known that the higher transition dipole moment always reveals stronger optical absorption. The Fig. 5(b) indicates that, when it is near VBM, the transition dipole moment along Y direction is very high while the transition dipole moment along X direction is very low, which can support the anisotropic optical absorption of monolayer CN_2.

Table 1 The electron and hole effective masses m_e^* and m_h^*, elastic modulus C_{2D} (eV Å^{-2}), deformation energies E_l (eV) and carrier mobilities μ (cm^2 V^{-1} s^{-1}) for monolayer CN_2 along X and Y directions at 300 K calculated by HSE06 hybrid functional

	m_X	m_Y	$E_l - X$	$E_l - Y$	$C_{2D} - X$	$C_{2D} - Y$	$\mu_{2D} - X$	$\mu_{2D} - Y$
e	0.24	0.67	36.12	6.71	33.26	27.17	88.4	754.1
h	7.76	0.69	3.13	3.10			303.6	1009.2

For further studying the photocatalytic properties of monolayer CN_2 for water splitting, its band edges alignment relative to vacuum level (VL) have been carried out after calculating its work function. And then, the VBM and CBM relative to VL have been compared with the H^+/H_2 reduction potential [$V(H^+/H_2) =$

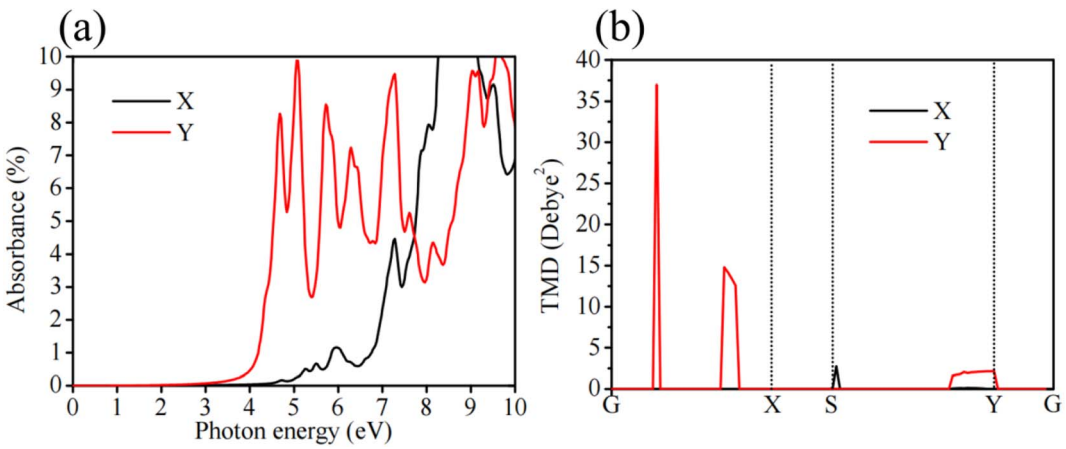

Fig. 5 (a) and (b) Are the optical absorption spectrum and transition dipole moment of monolayer CN_2, respectively.

© 2024 The Author(s). Published by the Royal Society of Chemistry

-4.44 eV + PH × 0.059 eV] and the OH^-/O_2 oxidation potential [$V(OH^-/O_2) = -5.67$ eV + PH × 0.059 eV] with considering the influence of PH values ranging from 0 to 14, as shown in Fig. 6(a). It presents that, when the PH values are ranging from 0 to 14, the VBM is higher than the $V(H^+/H_2)$ and the CBM is lower than the $V(OH^-/O_2)$, which means that monolayer CN_2 has potential on overall photocatalytic water splitting. In addition, it also exhibits that, with the increase of PH values, the overpotential $\chi(H_2)$ for H^+/H_2 reduction will decrease and while the overpotential $\chi(O_2)$ for the OH^-/O_2 oxidation will increase. Moreover, when the PH value is 7 corresponding to neutral water, the $\chi(H_2)$ and $\chi(O_2)$ are 0.37 eV and 1.24 eV, respectively, which indicates that monolayer CN_2 would have good photocatalytic activity in water splitting at PH = 7. As the band gap, $\chi(H_2)$ and $\chi(O_2)$ of monolayer CN_2 with considering PH values ranging from 0 to 14 were obtained, the corresponding solar to hydrogen (STH) efficiency have been calculated by following formulas:

The optical absorption efficiency (η_{ab}):[51–53]

$$\eta_{ab} = \frac{\int_{E_g}^{\infty} P(\hbar\omega)\mathrm{d}(\hbar\omega)}{\int_{0}^{\infty} P(\hbar\omega)\mathrm{d}(\hbar\omega)} \tag{10}$$

where the E_g is the band gap, and $P(\hbar\omega)$ is the AM 1.5G solar energy flux as functional of the photon energy$\hbar\omega$.

The efficiency of carrier utilization (η_{cu}):

$$\eta_{cu} = \frac{\Delta G \int_{E}^{\infty} \frac{P(\hbar\omega)}{\hbar\omega}\mathrm{d}(\hbar\omega)}{\int_{E_g}^{\infty} P(\hbar\omega)\mathrm{d}(\hbar\omega)} \tag{11}$$

where the ΔG is 1.23 eV describing the potential difference of water splitting, and E is the photon energy actually used for water splitting, which is defined as:

$$E = \begin{cases} E_g(\chi(H_2) \geq 0.2, \chi(O_2) \geq 0.6) \\ E_g + 0.2 - \chi(H_2)(\chi(H_2) < 0.2, \chi(O_2) \geq 0.6) \\ E_g + 0.6 - \chi(O_2)(\chi(H_2) \geq 0.2, \chi(H_2) < 0.6) \\ E_g + 0.8 - \chi(H_2) - \chi(O_2)(\chi(H_2) < 0.2, \chi(O_2) < 0.6) \end{cases} \tag{12}$$

The STH efficiency (η_{sth}):

$$\eta_{sth} = \eta_{ab} \times \eta_{cu} \tag{13}$$

The results, including the η_{ab}, η_{cu} and η_{sth}, are shown in Fig. 6(b). Learning from the Fig. 6(b), we can get that, when the PH = 0, 1 and 2, the η_{sth} have maximum values 9.6% for η_{sth}. And then, with the increase of PH values from 3 to 14, the η_{sth} will reduce. For instance, when PH = 7 and 14, the η_{sth} are 5.8% and 2.4%, respectively. The phenomenon is caused by that, when the PH values are ranging from 3 to 14, the values of η_{ab} will not be affected but the values of η_{cu} will decrease with the increase of PH values due to the $\chi(H_2)$ and $\chi(O_2)$ changing with the PH but the band gap not.

3.3 The strain effect on the band structure, optical absorption and photocatalytic properties of monolayer CN_2

Although the STH efficiency of monolayer CN_2 reach 9.6% at PH = 0, the performance of monolayer CN_2 in photocatalytic water splitting does not satisfy the requirement of economic hydrogen production, which needs the STH efficiency of photocatalysts beyond 10%. Thus, we have applying the uniaxial strain along X and Y direction to monolayer CN_2 shown in Fig. 7(a), which is expected to improve the photocatalytic ability of monolayer CN_2 in water splitting. The strain with negative sign represents compressive strain while the strain with positive sign means tension strain. The magnitude of strain means the ratio of the deformation of lattice parameter (a or b) to the original value. The Fig. 7(b) reveals the relation of stress to uniaxial strain, which can give a guide to the relevant experiment. Learning from Fig. 7(b), we find that the hardness of monolayer CN_2 along X direction is higher than that along Y direction and the tension strain is easier to achieve in monolayer CN_2 rather than compressive strain. In addition, it also exhibits that, under the compressive strain, the stress varies linearly, which means the potential of monolayer CN_2 on pressure sensors.

To study the strain effect on the photocatalytic properties of monolayer CN_2 in water splitting, we have first carried out the band structures that change with the uniaxial strain along X and

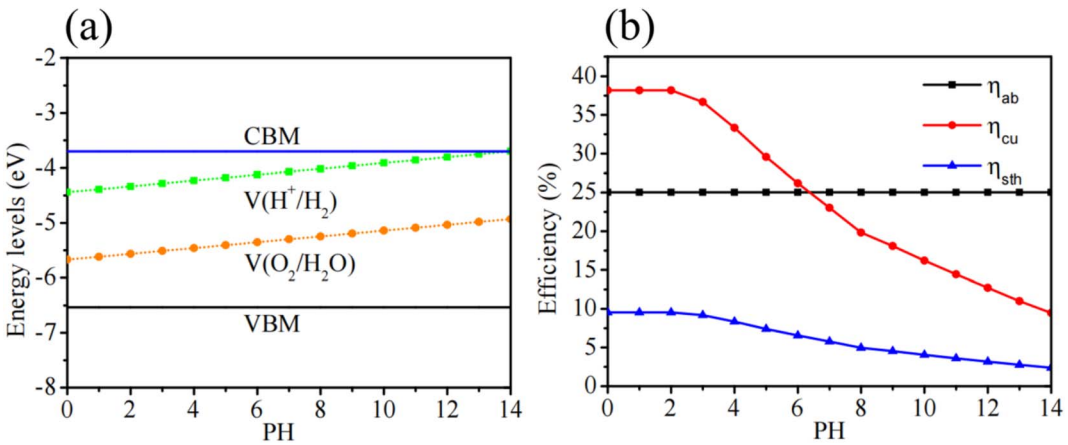

Fig. 6 (a) Is the VBM and CBM of monolayer CN_2 comparing with the redox potential water splitting at PH ranging from 0 to 14. (b) Is the optical absorption η_{ab}, carrier utilization η_{cu}, solar to hydrogen η_{sth} efficiency changing with the PH values.

© 2024 The Author(s). Published by the Royal Society of Chemistry

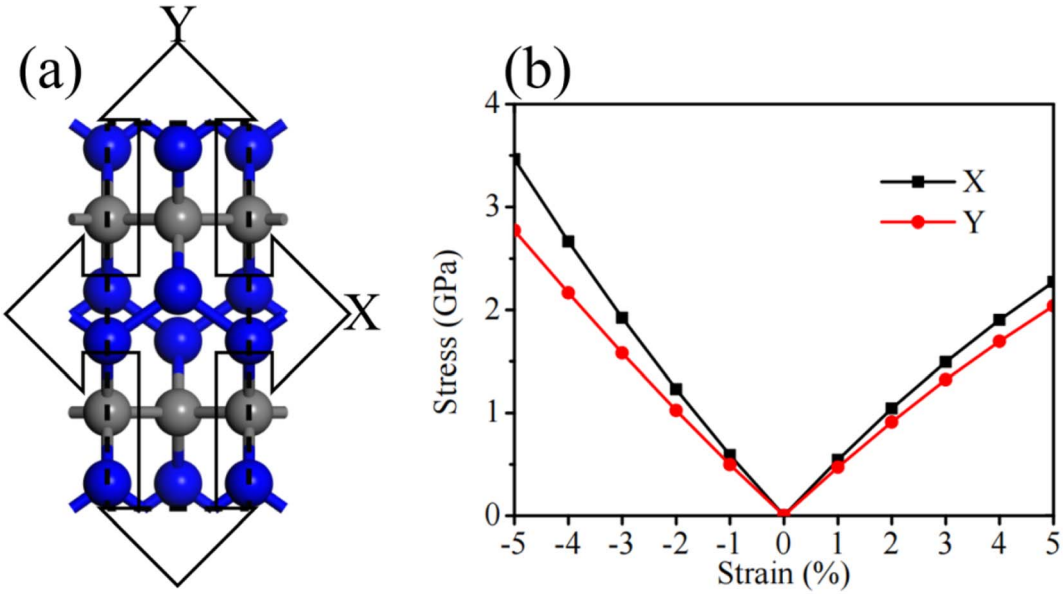

Fig. 7 (a) Is the schematic diagram for applying uniaxial strain to monolayer CN_2. (b) Is the stress of monolayer CN_2 changing with strain.

Y direction. The Fig. 8(a) exhibits the band gaps of monolayer monolayer CN_2 changing with the strain. It shows that, when the strain is ranging from −5% to 5% along *X* direction, the band gaps of monolayer CN_2 can be tuned from 1.322 eV to 3.713 eV. And when the strain is ranging from −5% to 5% along *Y* direction, the band gaps can be tuned from 2.309 eV to

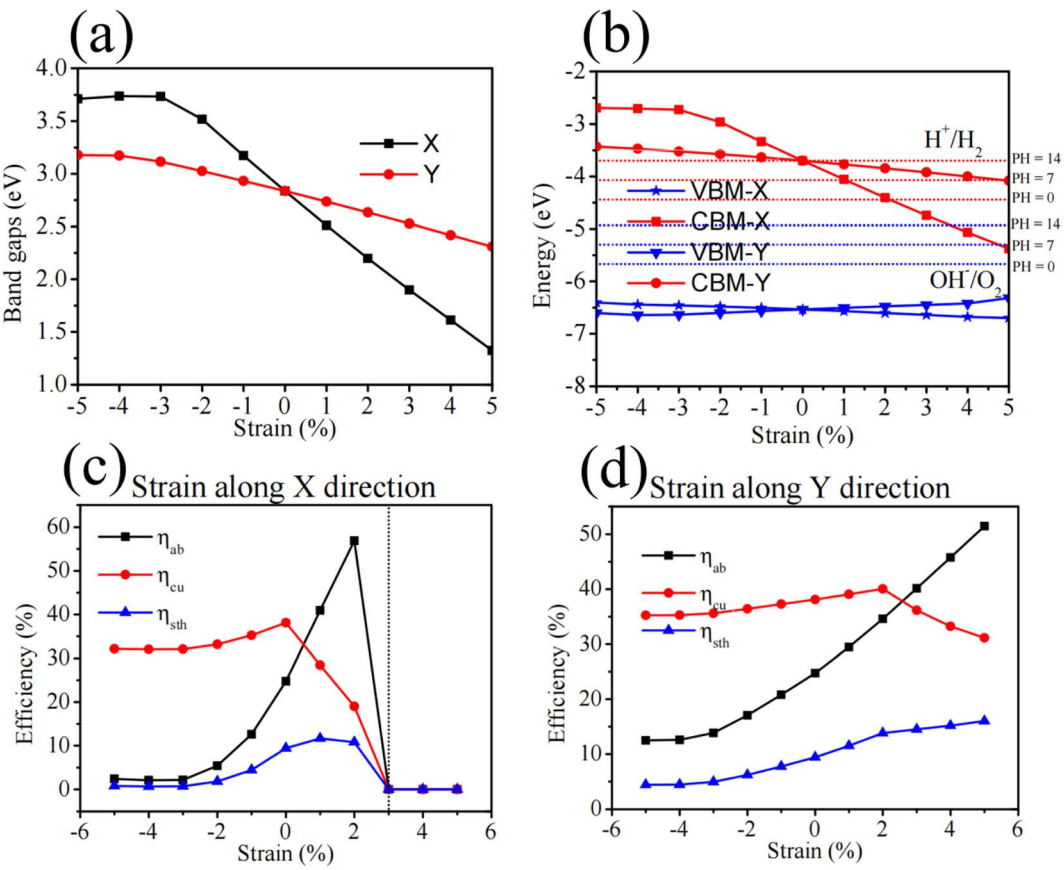

Fig. 8 (a) Is the band gaps of monolayer CN_2 changing with uniaxial strain. (b) Is the VBM and CBM of monolayer CN_2 under the uniaxial strain, comparing with the redox potential water splitting at $P = 0$, 7 and 14. (c) and (d) are the η_{ab}, η_{cu} and η_{sth} of monolayer CN_2 under uniaxial strain along *X* and direction, respectively.

© 2024 The Author(s). Published by the Royal Society of Chemistry

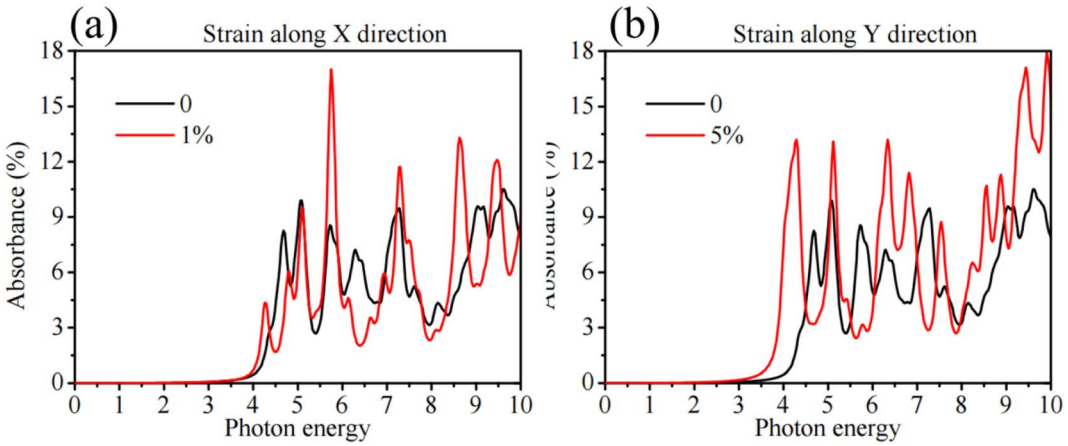

Fig. 9 (a) Is the optical absorption spectrum of monolayer CN_2 under 1% uniaxial tension strain along *X* direction comparing with that of monolayer CN_2 without strain. (b) Is the optical absorption spectrum of monolayer CN_2 under 5% uniaxial tension strain along *Y* direction comparing with that of monolayer CN_2 without strain.

3.178 eV. The phenomenon indicates that, compared with the strain along *Y* direction, the strain along *X* direction can more effectively control the band gap of monolayer CN_2 due to the VBM and CBM being mainly contributed by N atoms. In addition, when the strain is ranging from −3% to 5% either along *X* or *Y* direction, the variation trend of band gap is near-linear, which will facilitate the regulation according to the need of practical application. Furthermore, as shown in Fig. 8(b), we also have carried out the band edge alignment of monolayer CN_2 with the uniaxial strain. Compared with the oxidation reduction potential in water splitting at PH = 0, 7 and 14, we find that, with uniaxial strain compressive ranging from −5% to 0 whether along *X* and *Y* direction, the monolayer CN_2 still can satisfy the band structure requirement of photocatalytic water splitting at PH ranging from 0 to 14. When the uniaxial strain is tension along *X* direction, monolayer CN_2 can keep its photocatalytic ability in water splitting under 0–2% strain at PH = 0 and 0–1% strain at PH = 7. Additionally, under the 0–5% uniaxial tension strain along *Y* direction, monolayer CN_2 can keep its photocatalytic ability in water splitting at PH = 0 and PH = 7. Moreover, the Fig. 8(b) also indicates that, at PH = 14, the uniaxial tension strain whether along *X* and *Y* direction would make monolayer CN_2 not suitable for photocatalytic water splitting.

The η_{ab}, η_{cu} and η_{sth} of monolayer CN_2 at PH = 0 have been presented in Fig. 8(c and d) after obtaining the change of the band gap, $\chi(H_2)$ and $\chi(O_2)$ with the uniaxial strain. As shown in Fig. 8(c), although the η_{ab} and η_{cu} are not the highest values under 1% uniaxial tension strain along *X* direction, the monolayer CN_2 has optimal η_{sth} reaching 11.64%, which means that applying 1% uniaxial tension strain can make monolayer CN_2 own potential on economic hydrogen production. In addition, when it is uniaxial tension strain ranging from 1% to 5% along *Y* direction, the η_{sth} of monolayer CN_2 is beyond the 10% and increases with the increase of uniaxial tension strain. And under 5% uniaxial tension strain along *Y* direction, the η_{sth} of monolayer CN_2 can be up to 16.02%. Furthermore, we also have carried out the optical absorption spectra of monolayer CN_2 with 1% uniaxial tension strain along *X* direction and 5% uniaxial tension strain along *Y* direction, which make monolayer CN_2 have pretty η_{sth}. As shown in Fig. 9(a), under the 1% uniaxial tension strain along *X* direction, the optical absorption polarized along *Y* direction of monolayer CN_2 is red shift compared with that without strain. And the Fig. 9(b) shows that, with the 5% uniaxial tension strain along *Y* direction, the optical absorption of monolayer CN_2 is red shift and its first absorption peak become stronger than that without strain. Above phenomenons suggest that applying suitable uniaxial tension strain to monolayer CN_2 can effective improve the photocatalytic ability of monolayer CN_2 in water splitting.

4 Conclusion

In summary, we have theoretically proposed a kind of anisotropic monolayer carbon nitride – CN_2 *via* first-principles DFT. Through the calculations of cohesive energy, phonon dispersion spectrum and AIMD simulations at 300 K and 400 K, we confirm that monolayer CN_2 has high stability in energy, dynamics and thermodynamics. By using HSE06 functional, we find that monolayer CN_2 is wide-direct-band-gap semiconductor with 2.836 eV band gap. And it also exhibit that its band edge alignment relative to vacuum level satisfy the requirement of photocatalysts applied in water splitting at PH ranging from 0 to14. And the efficiency of solar to hydrogen in monolayer CN_2 is 9.6% at PH = 0. Due to the anisotropic structure, the monolayer CN_2 has anisotropic carrier mobility and optical absorption. And our calculations present that monolayer CN_2 has high electron mobility ($\sim 10^3$ cm^2 V^{-1} s^{-1}) and visible-ligh optical absorption along *Y* direction while that along *X* direction own poor performances. Finally, we have studied the uniaxial strain effect on the electronic, optical and photocatalytic properties of monolayer CN_2. And the results show that uniaxial strain can effectively tune the band gap, overpotential and optical absorption of monolayer CN_2, which can further control the photocatalytic ability for water splitting. Our calculations not only propose a kind of wide-direct-band-

© 2024 The Author(s). Published by the Royal Society of Chemistry

gap semiconductor for photocatalytic water splitting but also provide a potential functional component for forming type-I and scheme-Z heterojunction applied in photocatalytic water splitting.

Data availability

The data that support the findings of this study are available on request from the corresponding author "Jiahe Lin"upon reasonable request.

Conflicts of interest

There are no conflicts to declare.

Acknowledgements

This study was supported by the National Natural Science Foundation of China (Grant No. 12204195) and the Fujian Province Department of Science and Technology (China) (Grant No. 2020J05147).

References

1 M. Z. Rahman, C. W. Kwong, K. Davey and S. Z. Qiao, *Energy Environ. Sci.*, 2016, **9**, 709–728.
2 S. Mekhilef, R. Saidur and A. Safari, *Renew. Sustain. Energy Rev.*, 2011, **15**, 1777–1790.
3 M. Pelaez, N. T. Nolan, S. C. Pillai, M. K. Seery, P. Falaras, A. G. Kontos, P. S. M. Dunlop, J. W. J. Hamilton, J. A. Byrne, K. O'Shea, M. H. Entezari and D. D. Dionysiou, *Appl. Catal., B*, 2012, **125**, 331–349.
4 J. S. Lee, *Catal. Surv. Asia*, 2005, **9**, 217–227.
5 B. Luo, G. Liu and L. Wang, *Nanoscale*, 2016, **8**, 6904–6920.
6 T. Hisatomi, J. Kubota and K. Domen, *Chem. Soc. Rev.*, 2014, **43**, 7520–7535.
7 Z. Saleem, E. Pervaiz, M. U. Yousaf and M. B. K. Niazi, *Catalysts*, 2020, **10**, 464.
8 N. Kannan and D. Vakeesan, *Renew. Sustain. Energy Rev.*, 2016, **62**, 1092–1105.
9 Y. Li, Y.-L. Li, B. Sa and R. Ahuja, *Catal. Sci. Technol.*, 2017, **7**, 545–559.
10 T. Su, Q. Shao, Z. Qin, Z. Guo and Z. Wu, *ACS Catal.*, 2018, **8**, 2253–2276.
11 N. Fajrina and M. Tahir, *Int. J. Hydrogen Energy*, 2019, **44**, 540–577.
12 A. K. Singh, K. Mathew, H. L. Zhuang and R. G. Hennig, *J. Phys. Chem. Lett.*, 2015, **6**, 1087–1098.
13 K. Wenderich and G. Mul, *Chem. Rev.*, 2016, **116**, 14587–14619.
14 Q. Cai, M. Paulose, O. K. Varghese and C. A. Grimes, *J. Mater. Res.*, 2005, **20**, 230–236.
15 M. Z. Rahman, C. W. Kwong, K. Davey and S. Z. Qiao, *Energy Environ. Sci.*, 2016, **9**, 709–728.
16 J. K. Stolarczyk, S. Bhattacharyya, L. Polavarapu and J. Feldmann, *ACS Catal.*, 2018, **8**, 3602–3635.
17 C.-F. Fu, J. Sun, Q. Luo, X. Li, W. Hu and J. Yang, *Nano Lett.*, 2018, **18**, 6312–6317.
18 Z. Guo, J. Zhou, L. Zhu and Z. Sun, *J. Mater. Chem. A*, 2016, **4**, 11446–11452.
19 X. Yang and D. Wang, *ACS Appl. Energy Mater.*, 2018, **1**, 6657–6693.
20 V. Soni, P. Raizada, A. Kumar, V. Hasija, S. Singal, P. Singh, A. Hosseini-Bandegharaei, V. K. Thakur and V.-H. Nguyen, *Environ. Chem. Lett.*, 2021, **19**, 1065–1095.
21 N. Fajrina and M. Tahir, *Int. J. Hydrogen Energy*, 2019, **44**, 540–577.
22 S. Cao, X. Yan, Z. Kang, Q. Liang, X. Liao and Y. Zhang, *Nano Energy*, 2016, **24**, 25–31.
23 S. Wang, J. Zhang, B. Li, H. Sun and S. Wang, *Energy Fuels*, 2021, **35**, 6504–6526.
24 S. Nayak, G. Swain and K. Parida, *ACS Appl. Mater. Interfaces*, 2019, **11**, 20923–20942.
25 F. K. Kessler, Y. Zheng, D. Schwarz, C. Merschjann, W. Schnick, X. Wang and M. J. Bojdys, *Nat. Rev. Mater.*, 2017, **2**, 17030.
26 X. Li, R. Shen, S. Ma, X. Chen and J. Xie, *Appl. Surf. Sci.*, 2018, **430**, 53–107.
27 W.-J. Ong, L.-L. Tan, Y. H. Ng, S.-T. Yong and S.-P. Chai, *Chem. Rev.*, 2016, **116**, 7159–7329.
28 A. Mehtab, S. Banerjee, Y. Mao and T. Ahmad, *ACS Appl. Mater. Interfaces*, 2022, **14**, 44317–44329.
29 D. Zhao, Y. Wang, C.-L. Dong, Y.-C. Huang, J. Chen, F. Xue, S. Shen and L. Guo, *Nat. Energy*, 2021, **6**, 388–397.
30 A. Alarawi, V. Ramalingam and J.-H. He, *Mater. Today Energy*, 2019, **11**, 1–23.
31 J. Wen, J. Xie, X. Chen and X. Li, *Appl. Surf. Sci.*, 2017, **391**, 72–123.
32 D. Zhao, Y. Wang, C.-L. Dong, Y.-C. Huang, J. Chen, F. Xue, S. Shen and L. Guo, *Nat. Energy*, 2021, **6**, 388–397.
33 L. Lin, Z. Yu and X. Wang, *Angew. Chem., Int. Ed.*, 2019, **58**, 6164–6175.
34 P. Niu, L. Zhang, G. Liu and H.-M. Cheng, *Adv. Funct. Mater.*, 2012, **22**, 4763–4770.
35 Z. Zhao, Y. Sun and F. Dong, *Nanoscale*, 2015, **7**, 15–37.
36 S. Cao, J. Low, J. Yu and M. Jaroniec, *Adv. Mater.*, 2015, **27**, 2150–2176.
37 X. Cai, Z. Zhu, W. Yu, C. Niu, J. Wang, B. Wang, X. Li, L. Zhang, R. Zhao and Y. Jia, *Materials*, 2018, **11**, 1937.
38 N. Wang, G. Yang, H. Wang, R. Sun and C.-P. Wong, *Front. Chem.*, 2018, **6**, 440.
39 J. Tian, Z. Zhou, S. Zhang, Z. Li, L. Shi, Q. Li and J. Wang, *J. Mater. Chem. A*, 2021, **9**, 11753–11761.
40 L.-B. Shi, Y.-Y. Zhang, X.-M. Xiu and H.-K. Dong, *Carbon*, 2018, **134**, 103–111.
41 X. Zhou, W. Feng, S. Guan, B. Fu, W. Su and Y. Yao, *J. Mater. Res.*, 2017, **32**, 2993–3001.
42 J. Lin, T. Zhang, B. Zhang and X. Wang, *Appl. Surf. Sci.*, 2021, **542**, 148597.
43 G. Kresse and J. Furthmüller, *Phys. Rev. B: Condens. Matter Mater. Phys.*, 1996, **54**, 11169.
44 H. J. Monkhorst and J. D. Pack, *Phys. Rev. B: Solid State*, 1977, **16**(4), 1748–1749.

© 2024 The Author(s). Published by the Royal Society of Chemistry

45 J. P. Perdew, K. Burke and M. Ernzerhof, *Phys. Rev. Lett.*, 1996, **77**, 3865.
46 W. G. Hoover and B. L. Holian, *Phys. Lett. A*, 1996, **211**, 253–257.
47 J. Heyd, G. E. Scuseria and M. Ernzerhof, Hybrid functionals based on a screened Coulomb potential, *J. Chem. Phys.*, 2003, **118**, 8207–8215.
48 V. Wang, N. Xu, J.-C. Liu, G. Tang and W.-T. Geng, *Comput. Phys. Commun.*, 2021, **267**, 108033.
49 M. D. Segall, P. J. D. Lindan, M. J. Probert and C. J. Pickard, *J. Phys.: Condens. Matter*, 2002, **14**, 2717–2744.
50 K. Kaasbjerg, K. S. Thygesen and K. W. Jacobsen, *Phys. Rev. B: Condens. Matter Mater. Phys.*, 2012, **85**, 115317.
51 M. Sun and U. Schwingenschlögl, *Chem. Mater.*, 2020, **32**, 4795–4800.
52 C.-F. Fu, J. Sun, Q. Luo, X. Li, W. Hu and J. Yang, *Nano Lett.*, 2018, **18**, 6312–6317.
53 J. Lin, T. Zhang, B. Zhang and X. Wang, *Appl. Surf. Sci.*, 2021, **542**, 148597.

© 2024 The Author(s). Published by the Royal Society of Chemistry